Editors' Suggestion

Dirac nodal lines protected against spin-orbit interaction in IrO_2

J. N. Nelson,[1] J. P. Ruf,[1] Y. Lee,[1] C. Zeledon,[2] J. K. Kawasaki,[3] S. Moser,[4] C. Jozwiak,[5] E. Rotenberg,[5] A. Bostwick,[5] D. G. Schlom,[2,6] K. M. Shen,[1,6,*] and L. Moreschini[2,†]

[1]*Laboratory of Atomic and Solid State Physics, Department of Physics, Cornell University, Ithaca, New York 14853, USA*
[2]*Department of Materials Science and Engineering, Cornell University, Ithaca, New York 14853, USA*
[3]*Department of Materials Science and Engineering, University of Wisconsin, Madison, Wisconsin 53706, USA*
[4]*Physikalisches Institut, Universität Würzburg, D-97074 Würzburg, Germany*
[5]*Advanced Light Source, Lawrence Berkeley National Laboratory, Berkeley, California 94720, USA*
[6]*Kavli Institute at Cornell for Nanoscale Science, Ithaca, New York 14853, USA*

(Received 8 April 2019; published 18 June 2019)

The interplay between strong spin-orbit coupling and electron correlations has recently been the subject of intense investigation, due to a number of theoretically predicted phases such as quantum spin liquids, unconventional superconductivity, complex magnetic orders, and correlated topological phases of matter. In particular, iridates have been proposed as a promising family of materials which could host a number of these phases. Here we report the existence of Dirac nodal lines in the binary oxide IrO_2, through a combination of reactive oxide molecular beam epitaxy and angle-resolved photoemission spectroscopy. Unlike in other such materials reported to date, these Dirac nodal lines have the unique property of being simultaneously (i) robust against spin-orbit coupling, as they are protected by the nonsymmorphic symmetry of the rutile structure, and (ii) only partially occupied, since they cross the Fermi level. This should have direct implications on the low-energy physics properties tied to the band velocity such as magnetoresistance and spin Hall effect.

DOI: 10.1103/PhysRevMaterials.3.064205

I. INTRODUCTION

Transition metal oxides have been widely studied over the past three decades owing to their unprecedented variety of electronic and magnetic properties including high temperature and unconventional superconductivity, metal-insulator transitions, multiferroicity, and colossal magnetoresistance, which arise due to electron correlations between partially filled *d* orbitals [1]. Despite their heterogeneity, few oxides have been shown to harbor unusual topological properties. Indeed, the vast majority of topological insulators, Dirac semimetals, and Weyl semimetals have been reported in intermetallic compounds [2–5], where calculations based on density functional theory (DFT) generally provide an accurate description of the electronic structure. It has been a major goal in condensed matter to achieve topological states where the topological protection is combined with the complex electronic and magnetic orders often present in oxides.

In this respect, iridates have been one of the main targets of investigation. As notable examples, the $R_2Ir_2O_7$ pyrochlores, where R is a rare-earth element, have been proposed to be Weyl semimetals or, under some conditions, axion insulators [6], while $SrIrO_3$ is predicted to be a topological crystalline metal with nodal rings [7]. Na_2IrO_3 and Li_2IrO_3 could provide the realization of the Kitaev quantum spin liquid model, which would harbor topological excitations such as Majorana fermions [8,9]. Finally, Sr_2IrO_4 has been demonstrated to be a spin-orbit-assisted Mott insulator [10] with intriguing similarities to the cuprate superconductors [11,12]. Nevertheless, the topological properties of many of these iridates remain difficult to identify, due in large part to the combination of spin-orbit and Coulomb interactions which makes first-principle calculations challenging, and to this point there exist no iridate compound whose topological nature has been conclusively determined.

The electronic structure of the rutile oxide IrO_2 has been relatively poorly studied by angle-resolved photoemission spectroscopy (ARPES) in comparison to other members of the family. The shortage of photoemission data is due in particular to the challenges in preparing high quality single crystals and to the lack of a natural cleavage plane. Like other iridates, IrO_2 also exhibits a number of interesting properties including a large spin Hall effect [13], a Hall effect where the carriers can be switched from electrons to holes by an applied magnetic field [14], as well as being an efficient catalyst [15,16]. It shares with the rest of the family the fundamental building blocks, the IrO_6 octahedra with the Ir^{4+} ion in a $5d^5$ configuration, which in IrO_2 are connected in a combination of corner- and edge-sharing neighbors [Fig. 1(a)]. It was recently predicted by Sun *et al.* to host band crossings protected along continuous lines in reciprocal space, called Dirac nodal lines (DNLs) [17], which in general result from a combination of time-reversal symmetry and crystal symmetries [18]. While in the majority of cases the theoretically predicted DNLs are not realized in practice due to spin-orbit coupling (SOC) opening a gap at the crossing point, in IrO_2 the nonsymmorphic symmetry of the crystal protects the band degeneracy along the nodal lines.

*kmshen@cornell.edu
†lmoreschini@cornell.edu

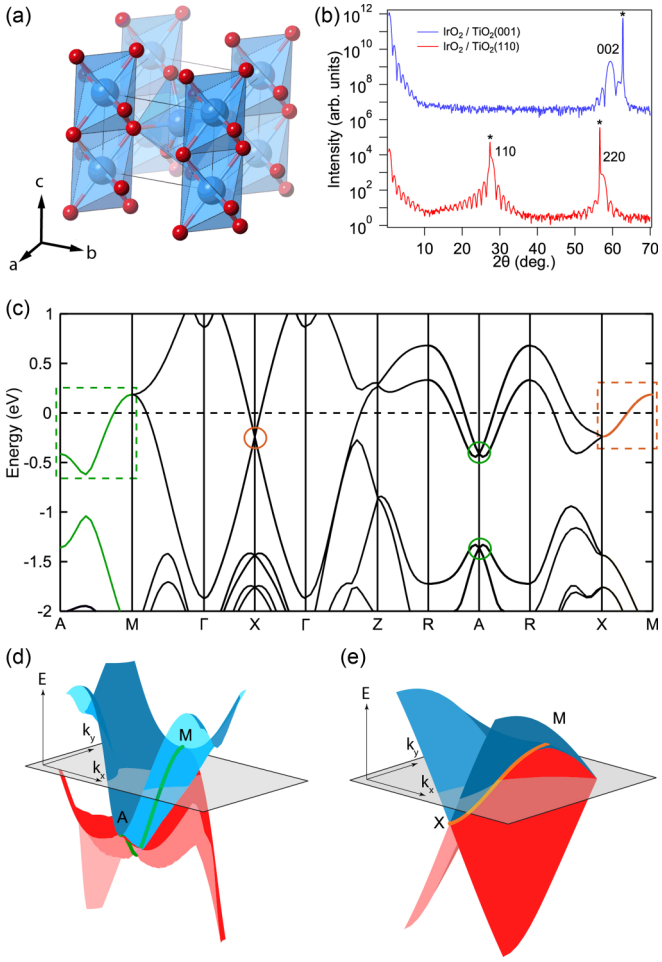

FIG. 1. (a) Crystal structure of IrO_2 and (b) x-ray diffraction θ-2θ scans exhibiting clear thickness fringes from ∼15 nm thick IrO_2(110) and IrO_2(001) films. The asterisks mark the TiO_2 substrate peaks. (c) The calculated band structure by GGA + SOC along a selected high symmetry path. The nodal lines discussed in this work are marked by the dashed boxes. The Γ-*X* and *R*-*A* directions normal to the lines are shown twice for representing the characteristic Dirac crossings, marked by circles superposed to the band structure. Every path perpendicular to the DNLs will show such a a crossing point, as apparent in the 3D renderings of the band structure along *A*-*M* (d) and *X*-*M* (e) where the gray planes represent the location of the Fermi level. The higher binding energy nodal line along *A*-*M* is not the focus of this work. It is not relevant for the low energy physics since it lies >1 eV from the Fermi level, and is likely to be difficult to measure accurately due to the broader ARPES linewidth at higher binding energy.

II. METHODS

A. Film growth, characterization, and ARPES measurements

This study is a combination of reactive oxide molecular-beam epitaxy (MBE) synthesis and ARPES. In order to reveal the nodal lines along multiple directions in the reciprocal space, thin films were grown on different surfaces.

Epitaxial (110) and (001) oriented IrO_2 films were grown on single-crystal TiO_2(110) and (001) substrates respectively [see Fig. 1(b) for an x-ray diffraction Cu $K\alpha$ $\theta/2\theta$ scan, demonstrating high crystalline quality of both films]. Samples between 5 and 20 nm were grown at 300 °C in a background pressure of 1×10^{-6} distilled ozone. Immediately after growth a single monolayer of crystalline TiO_2 (∼1.5 Å) was deposited as a protective cap under the same conditions. Samples were transported in low vacuum and annealed at 350 °C in 2×10^{-5} Torr of 10% ozone prior to measurement. This process removes adsorbed contaminants from the surface, but does not remove the TiO_2 cap, as demonstrated by the post annealing x-ray photoemission spectroscopy (XPS) data shown in Fig. S3. The XPS Ti 2*p* signal is expected to originate from the overlayer only since all samples had a thickness of at least 5 nm, much larger than the inelastic mean free path of electrons at a kinetic energy of 600 eV [19]. Note that since TiO_2 has a wide band gap [20,21] we do not expect to see in photoemission any contribution from the overlayer in the vicinity of the Fermi level. Further details on the film growth and characterization are available in the Supplemental Material [22].

ARPES measurements over the full three-dimensional (3D) Brillouin zone (BZ) were undertaken at the MAESTRO beamline at the Advanced Light Source using a photon energy of 84–140 eV, with a combined resolution of 15 to 25 meV depending on the photon energy, at temperatures of approximately 70 K. For the experimental geometry see Fig. S5 in Ref. [22].

B. DFT calculations

Nonmagnetic DFT calculations were performed using the Quantum ESPRESSO software package [23] using fully relativistic, norm-conserving pseudopotentials for Ir and O [24]. We represented the Kohn-Sham wave functions in a basis set of plane waves extending up to a kinetic energy cutoff of 80 Ry, and used a cutoff of 320 Ry for representing the charge density. An $8 \times 8 \times 12$ *k* mesh was used for Brillouin zone integrations along with Gaussian smearing for band occupations. Perdew-Burke-Ernzerhof parametrization of the generalized gradient approximation (GGA) was employed as the exchange-correlation functional [25]. To ensure that our calculations accurately capture the effects of sizable spin-orbit coupling inherent to iridates, we cross-checked these results against those computed using the full-potential (linearized augmented plane wave plus local orbitals) WIEN2k code [26] and observed negligible differences in the band energies near the Fermi level. After obtaining self-consistent Kohn-Sham eigenstates via DFT, we used the Pw2wannier and Wannier90 codes [27] to construct 20 Wannier functions spanning the manifold of eigenstates surrounding E_F (ten *d* orbitals per Ir atom times two Ir atoms per unit cell).

III. RESULTS

A. Crystal symmetry and electronic structure

Figure 1(c) shows the band structure along selected high symmetry directions, as obtained by DFT in the GGA approximation including SOC. The results are consistent with the band structure published in Refs. [17,28]. Along *A*-*M* and *X*-*M* the dispersion consists of a single curve, where for space group No. 136 a nonsymmorphic term adds an additional symmetry to the usual time and space inversions, and as a

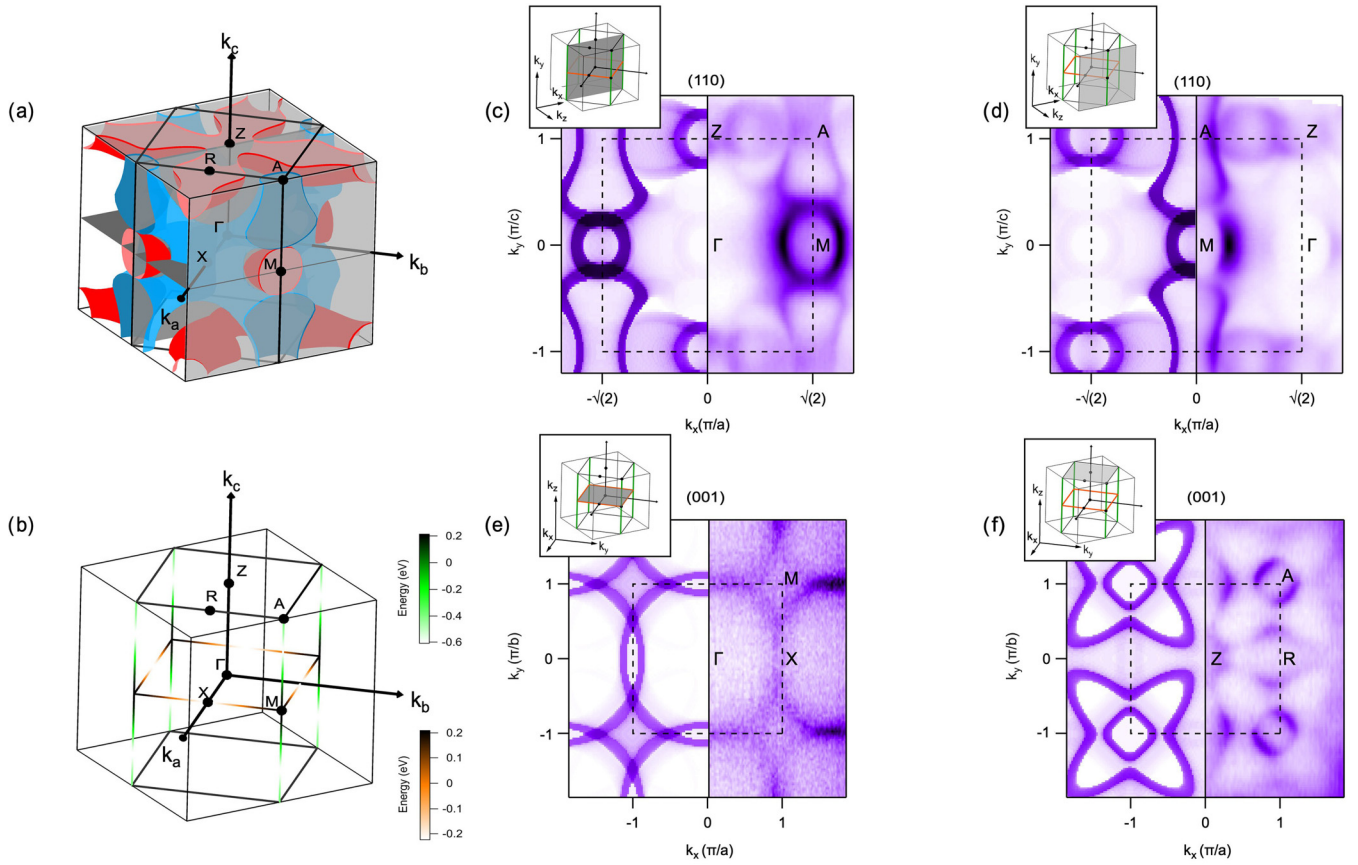

FIG. 2. (a) 3D rendering of the calculated Fermi surface, with holelike bands in red and electronlike bands in blue. The gray planes correspond to the BZ center and BZ boundary for the [110] and [001] orientations, and indicate the location of the Fermi surfaces measured by ARPES in (c)–(f), as shown in the insets. (b) The 3D BZ with high symmetry directions hosting the DNLs object of this study, shown in green for the A-M line and orange for the X-M line. The energy of the band along the k path is color coded as shown. The photon energies used are (c) 124 eV, (d) 84 eV, (e) 140 eV, and (f) 100 eV, and the inner potential V_0 used is 11.5 eV for (110) and 4 eV for (001) films, respectively. The sample temperature was ∼70 K. On the left half of (c)–(f), the calculated Fermi surfaces are shown with a k_z broadening of 0.2 Å^{-1}. For bulk IrO_2, $\pi/a = \pi/b \simeq 0.70$ Å^{-1}, $\pi/c \simeq 1.00$ Å^{-1}. The experimental data show a slight mismatch with the drawn bulk BZs in view of the strain on films. In all ARPES plots and in the text we name xy the sample surface plane and z the axis normal, for both orientations. As a consequence, k_z is the out of plane momentum regardless of the surface.

consequence the band degeneracy increases from double to fourfold. Namely, the combination of a translation of half the body diagonal τ and a fourfold rotational symmetry around the c axis provides the degeneracy along A-M [Fig. 1(d)], while the combination of τ and mirror symmetry with respect to the a axis is responsible for that along X-M [Fig. 1(e)].

B. Comparison to DFT

The choice of the sample orientation for measuring the DNLs is in principle arbitrary, but because of the strong photon energy dependence of the photoemission intensity in IrO_2 we choose to measure A-M and X-M on the (110) and (001) surface, respectively, where they can be followed at constant $h\nu$.

The calculated 3D Fermi surface is shown in Fig. 2(a), and consists of two sheets of holelike states (red) and one of electronlike states (blue). The reciprocal space locations of the nodal lines are shown in Fig. 2(b), with the A-M line in green and the X-M line in orange, the latter forming closed loops. It is apparent that the A-M line is more naturally accessible by ARPES on the (110) surface, as the whole line can be measured at a single photon energy, while the X-M line is more easily measured on the (001) surface. This motivates the synthesis and measurement of these two orientations of IrO_2. In Figs. 2(c) and 2(d) and Figs. 2(e) and 2(f) we show the measured Fermi surfaces for (110) and (001) films, respectively, at the center [Figs. 2(c) and 2(e)] and at the boundary [Figs. 2(d) and 2(f)] of the BZ, compared to simulated Fermi surface maps from DFT with an added k_z broadening of 0.2 Å^{-1}. Aside from a slight discrepancy between the relative sizes of the hole and electron pockets in the (110) surface, the experimental results match with the DFT predictions, with no observable surface states as opposed to what previously claimed [29] (this point is further clarified in Fig. S4). Considering the importance of correlations in partially filled d orbitals, it is not *a priori* guaranteed that a DFT approach is a good starting point, and therefore the presence of such agreement is not a trivial observation.

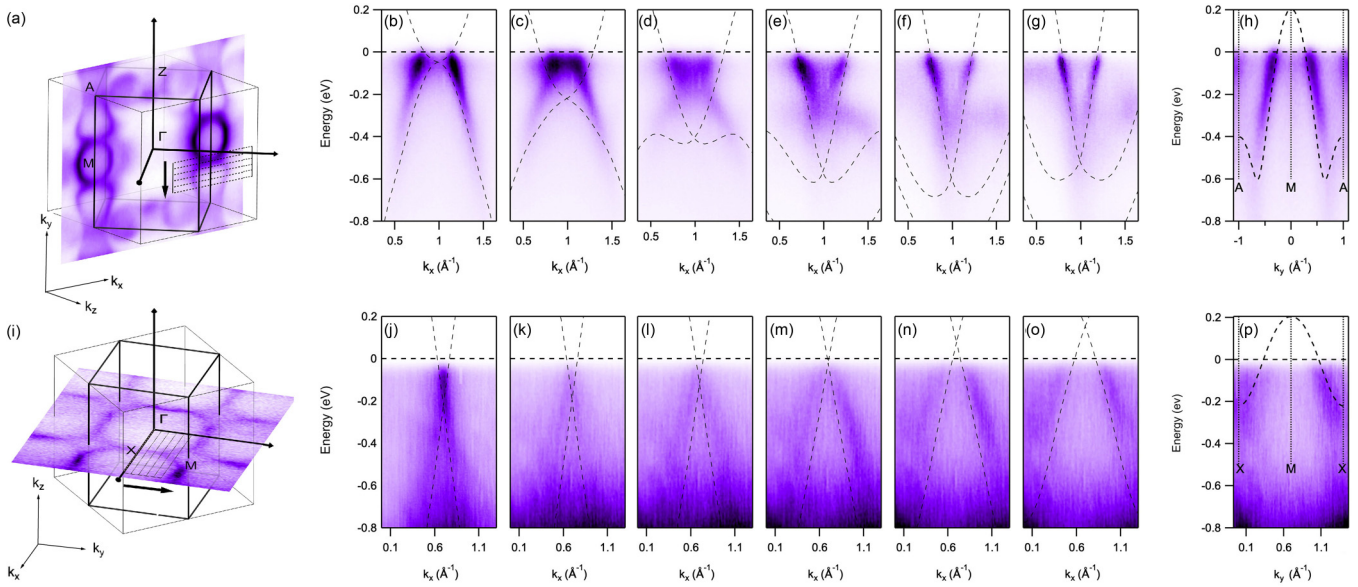

FIG. 3. (a) The Fermi surface for the (110) surface at the BZ center, from Fig. 2(b). The dashed lines and the arrow indicate the locations of the dispersion images for the data in (b)–(g), where the DFT results are superposed as dashed curves. (i) and (j)–(o) The equivalent of (a) and (b)–(g) for the (001) surface. (h) and (p) The nodal line dispersion along *A*-*M*-*A* and *X*-*M*-*X*, respectively. The sample temperature was ∼70 K. The photon energy is 124 eV for *A*-*M* and 140 eV for *X*-*M*.

The results shown in Figs. 2(c) and 2(d) are consistent with earlier ARPES measurements on IrO_2(110) [28,29], though the present data are the most extensive to date and the first ones on IrO_2(001). In regards to these constant energy maps, it is worthwhile to note that the ARPES intensity is fairly isotropic with *p* polarization, but shows a clear suppression in *s* polarization along the k_x and k_y axes, as we show in Fig. S5 for the Fermi surface measured on (110) at the *M* point. This is immediate consequence of some degree of orbital ordering in IrO_2 [30], as opposed to the perovskite iridates where the orbital momentum *L* is not a good quantum number and ARPES shows no dipole matrix element effects [10]. The minor role of correlations in IrO_2 in comparison with other iridates is believed to stem from the different arrangement and higher connectivity of the octahedra in the rutile structure [28,30].

C. Evolution of the nodal lines

In Fig. 3 we focus more directly on the measurement of the nodal lines, starting from the *A*-*M* direction in the (110) sample. In Fig. 3(a) the Fermi surface of Fig. 2(c) is inserted in the 3D BZ. The dashed lines mark the locations of the *E* vs k_x images (with k_x normal to the plane containing the DNL) shown in Figs. 3(b)–3(g), in direction of *M* to *A* as indicated by the arrow. The ensuing nodal line dispersion is shown in the *E* vs k_y image of Fig. 3(h). The DFT bands are superposed to the data for clarity. Near *M* the electronic states are unoccupied as the Fermi surface consists of a hole pocket. Taking cuts in direction of *A*, the crossing point moves to and below the Fermi level. The band dispersion in the vicinity of the crossing point becomes less clear towards *A* where it is further from the Fermi level. Because of the aforementioned underestimation of the hole pockets, the theory agrees with the data but with a mismatch in the binding energy of the crossing point (the mismatch is large enough that the Fermi level crossing of the Dirac node in DFT is outside the range shown here for the *A*-*M* line). Figures 3(j)–3(o) are the correspondents of the top panels, now for the *X*-*M* line, with the Fermi surface from Fig. 2(e) inserted in Fig. 3(i). The Fermi surface is slightly electronlike at *X*, with a crossing point at ∼50 meV binding energy, and evolves into the holelike sheet at *M*. The nodal line dispersion is shown Fig. 3(p). The band dispersion at the crossing points is not guaranteed to be linear over a large energy range, and while in some cases a roughly linear dispersion extends over more than 1 eV [31], in others the dispersion has a higher order term at all energies [32]. In IrO_2 the linear dispersion is clearly visible over several hundreds of meV only along *X*-*M*, while along *A*-*M* the bands appear parabolic all the way to the crossing point.

Within the limitations dictated by the experimental broadening of the linewidth, we cannot find the presence of any gap in either nodal line. Also the dispersion along *R*-*A*-*R* measured on the (001) surface, where the dispersion can be more easily followed, clearly hints at a gapless crossing at *A* (see Fig. S6). On this point, note that, as opposed to the many instances of quasi 2D materials hosting Dirac crossings, more sophisticated analysis methods aiming to exclude the presence of a gap in bulk states of 3D systems do not seem, in general, justified. Due to the finite escape depth of photoelectrons, ARPES data present an intrinsic k_z broadening. Using a reasonable value of $\lambda = 5$ Å for the electron mean free path, we obtain an approximate k_z distribution over $1/\lambda = 0.2$ Å^{-1} [33]. For IrO_2, along both nodal lines, at a k_z value 0.1 Å^{-1} away from the Dirac node, a gap larger than 50 meV is expected (see Fig. S7). The strict identification of a crossing point in bulk states is therefore not possible, and the presence of a single peak depends on the exact k_z dispersion

in the vicinity of the node and on other (extrinsic) broadening factors. In addition to the above, whereas growth on the (001) surface preserves the space group symmetry, in (110) films the surface epitaxial strain distorts the rutile structure, breaking the symmetry terms which protect the nodal lines. For a unit cell distortion by ∼2% along $[1\bar{1}0]$, ∼−5% along [001], and ∼0.8% along [110] (normal to the surface plane), as inferred by x-ray diffraction (see Ref. [22]), DFT predicts an opening of a gap as large as ∼50 meV depending on the parallel momentum, as shown in Fig. S9.

IV. DISCUSSION

There is an apparent difference between the electronic structure of IrO_2 and that of the other DNL materials reported so far. Both nodal lines here have a large energy dispersion (∼0.5 eV) and they cross the Fermi level, making it a unique case. As an immediate consequence, any contribution to the low energy physics can be expected to be robust against perturbations which shift the chemical potential.

Nodal lines may be categorized on the basis of which symmetry terms are at their origin, with some compounds believed to host more than a single type. When time-reversal symmetry is required for its existence, by definition the nodal line is not robust against SOC. The lifting of the degeneracy can be minor in materials with a small spin-orbit term [34–36], but dramatic in those containing heavy elements [37,38]. Protection from SOC requires an additional symmetry other than space inversion, namely a nonsymmorphic term in the crystal space group [18] (a separate case is the one of Weyl nodal lines, which are protected by mirror symmetry and where the spin components are split by broken time or space inversion symmetry [39]). The accepted examples of DNLs protected by nonsymmorphic symmetry are mostly found in crystals of the $P4/nmm$, No. 129 space group, namely the family of Zr(Hf)SiX compounds (X=S, Se, Te) [31,40–42] and InBi [43], whereas IrO_2 crystallizes in space group No. 136. A number of others have been predicted [44,45] but not yet experimentally verified.

In contrast to IrO_2, however, both in InBi and in the Zr(Hf)SiS family the nonsymmorphic symmetry protected DNL along X-R is far below the Fermi level, making it out of reach for low energy excitations [43,46]. The nodal lines lying on the natural (001) cleaving plane, on the other hand, show a small dispersion along the characteristic diamond-shaped Fermi surface and are unstable against SOC, with a gap opening from ∼20 meV to several tens of meV depending on the spin-orbit term of the atomic species in the crystal. In ZrSiTe the X-R line is instead believed by theory to lie much closer to the Fermi level, but it could not be seen in experiments, possibly because of natural hole doping in this family of layered crystals [42].

A separate mention deserves the case of RuO_2, which is isostructural to IrO_2 and was recently found to host a nodal line along the X-R high symmetry direction, crossing the Fermi level [47]. Although there is no symmetry protection along X-R, the small SOC of Ru (∼0.13 vs ∼0.41 eV) relative to Ir [48], together with the obligated fourfold degeneracy at X, makes it so that the gap is only a few meV in the vicinity of X, where the Fermi level crossing occurs. This provides a useful term of comparison between a material with low energy states consisting of a DNL strictly protected against SOC, and one with a very similar band structure but with lifted degeneracy, albeit by a small gap. How much influence such perturbation may have on the low energy properties is an open question, and it is argued by several authors that in materials with light elements the effect of SOC on the DNL could be considered in practice negligible [34,36].

The comparison is particularly relevant between IrO_2 and RuO_2 since the two are widely studied in electrochemistry for water splitting. In RuO_2(110) a surface state pinned to the nodal line was observed, but its role for photocatalysis remains uncertain since IrO_2 shows a similar activity ratio [49] but does not host any surface state. Also, the influence on chemistry of the details of the band structure at a given orientation seems difficult to reconcile with the higher efficiency reported in amorphous compared to rutile RuO_2 films [50].

IrO_2 was shown to exhibit large magnetoresistance [51,52], for which a key quantity is the electron mobility, and therefore the band velocity. It is difficult to infer a reliable Fermi velocity for the A-M DNL where the carriers are massive except for a small region around the crossing point. In contrast, the band velocity in the X-M DNL along the Γ-X direction is linear over a large range [Fig. 3(j)], and we extract $hv_F \simeq 3.1$ eV Å, a large value, higher than ∼2 eV Å in RuO_2 [47], comparable to ∼3–5 eV Å for the Dirac crossing at X in Zr(Hf)SiS [31,42] and about half of ∼6.5 eV Å in graphene [53]. These considerations altogether hint at the possibility that IrO_2 may be a viable candidate for magnetoresistive devices. However, the large variations observed within the different DNL compounds—the magnetoresistance in IrO_2 [51,52] is larger than in good conductors such as noble or alkali metals [54], but at least two orders of magnitude smaller than in ZrSiS [55,56], and at least three orders of magnitude smaller than in the WP_2 and MoP_2 Weyl semimetals [54], all layered, quasi-2D compounds—clearly indicates that the presence of massless fermions is not linked to the magnetotransport properties in a straightforward way and is instead strongly dependent on the fermiology of the material.

This work has shown that the binary oxide IrO_2 has an exotic electronic structure consisting of a network of intersecting nodal lines along A-M and X-M where the band crossings are protected by nonsymmorphic symmetry against strong SOC. These nodal lines are unusual in that they disperse strongly in energy and cross the Fermi level. Some aspects make IrO_2 a nontrivial target for further work aiming to tune and explore new topological properties. The rutile structure is more three dimensional and therefore (i) has a more complex fermiology, and (ii) is less prone to modular heterostructuring where electronic properties can be altered and engineered with strain and confinement, with respect to layered compounds such as perovskites. In view of studying the interplay of SOC-driven topological phases and correlations [6], it lies in the weak correlation limit due to the large (∼3 eV) bandwidth of its t_{2g} states. Nonetheless, aside from the important differences established above with respect to the DNL compounds discovered so far, IrO_2 is an exciting playground for this field in that it is a simple binary transition metal oxide, already widely

studied for practical applications. It can be grown epitaxially at low temperatures, making it suitable for integration in more complex architectures. This is in contrast to the other iridates, which have complex crystal structures and are in general difficult to synthesize.

A fascinating direction to pursue in the future is to identify clearer connections between the band structure of IrO_2 and its macroscopic properties such as the large spin Hall effect or magnetoresistance, or yet its efficiency in catalysis. There are no established links between these at the moment, and working on epitaxial films allows for additional tuning parameters by exposing different crystal planes and imparting strain. As an example, it is an interesting question, which requires further investigation, how sizable the effect of the crystal distortion in the (110) orientation is on the low energy properties such as the large spin Hall effect [13]. Recent work on the predicted nodal line material $SrIrO_3$, for example, points to a determinant role played by the nonsymmorphic symmetry term, in lack of which, such as under epitaxial strain, the spin Hall conductivity decreases [57].

Note added: After submission of this work, another article appeared on IrO_2(110) single crystals, in qualitative agreement with most of our findings [58].

ACKNOWLEDGMENTS

We gratefully acknowledge discussions with Alberto Crepaldi, Christian R. Ast, and Jin Suntivich. L.M. thanks Helmut Berger, Arnaud Magrez, and Philippe Bugnon for providing IrO_2 single crystals for preliminary measurements. This work was supported through the National Science Foundation [Platform for the Accelerated Realization, Analysis, and Discovery of Interface Materials (PARADIM)] under Cooperative Agreement No. DMR-1539918, NSF DMR-1709255, and the Air Force Office of Scientific Research Grant No. FA9550-15-1-0474. J.N.N. acknowledges support from the NSF Graduate Research Fellowship under Grant No. DGE-1650441. This research used resources of the Advanced Light Source, which is a DOE Office of Science User Facility under Contract No. DE-AC02-05CH11231. This work made use of the Cornell Center for Materials Research Shared Facilities which are supported through the NSF MRSEC program (DMR-1719875). Substrate preparation was performed in part at the Cornell NanoScale Facility, a member of the National Nanotechnology Coordinated Infrastructure (NNCI), which is supported by the NSF (Grant No. ECCS-1542081). Some images were generated using CrystalMaker®: CrystalMaker Software Ltd. (www.crystalmaker.com).

[1] J. Ngai, F. Walker, and C. Ahn, Annu. Rev. Mater. Res. **44**, 1 (2014).

[2] Z. K. Liu, B. Zhou, Y. Zhang, Z. J. Wang, H. M. Weng, D. Prabhakaran, S.-K. Mo, Z. X. Shen, Z. Fang, X. Dai, Z. Hussain, and Y. L. Chen, Science **343**, 864 (2014).

[3] M. Neupane, S.-Y. Xu, R. Sankar, N. Alidoust, G. Bian, C. Liu, I. Belopolski, T.-R. Chang, H.-T. Jeng, H. Lin, A. Bansil, F. Chou, and M. Z. Hasan, Nat. Commun. **5**, 3786 (2014).

[4] J. A. Logan, S. J. Patel, S. D. Harrington, C. M. Polley, B. D. Schultz, T. Balasubramanian, A. Janotti, A. Mikkelsen, and C. J. Palmstrøm, Nat. Commun. **7**, 11993 (2016).

[5] Z. K. Liu, L. X. Yang, S. C. Wu, C. Shekhar, J. Jiang, H. F. Yang, Y. Zhang, S. K. Mo, Z. Hussain, B. Yan, C. Felser, and Y. L. Chen, Nat. Commun. **7**, 12924 (2016).

[6] W. Witczak-Krempa, G. Chen, Y. B. Kim, and L. Balents, Annu. Rev. Condens. Matter Phys. **5**, 57 (2014).

[7] J.-M. Carter, V. V. Shankar, M. A. Zeb, and H.-Y. Kee, Phys. Rev. B **85**, 115105 (2012).

[8] S. Hwan Chun, J.-W. Kim, J. Kim, H. Zheng, C. C. Stoumpos, C. D. Malliakas, J. F. Mitchell, K. Mehlawat, Y. Singh, Y. Choi, T. Gog, A. Al-Zein, M. M. Sala, M. Krisch, J. Chaloupka, G. Jackeli, G. Khaliullin, and B. J. Kim, Nat. Phys. **11**, 462 (2015).

[9] T. Takayama, A. Kato, R. Dinnebier, J. Nuss, H. Kono, L. S. I. Veiga, G. Fabbris, D. Haskel, and H. Takagi, Phys. Rev. Lett. **114**, 077202 (2015).

[10] B. J. Kim, H. Jin, S. J. Moon, J.-Y. Kim, B.-G. Park, C. S. Leem, J. Yu, T. W. Noh, C. Kim, S.-J. Oh, J.-H. Park, V. Durairaj, G. Cao, and E. Rotenberg, Phys. Rev. Lett. **101**, 076402 (2008).

[11] Y. K. Kim, O. Krupin, J. D. Denlinger, A. Bostwick, E. Rotenberg, Q. Zhao, J. F. Mitchell, J. W. Allen, and B. J. Kim, Science **345**, 187 (2014).

[12] Y. K. Kim, N. H. Sung, J. D. Denlinger, and B. J. Kim, Nat. Phys. **12**, 37 (2016).

[13] K. Fujiwara, Y. Fukuma, J. Matsuno, H. Idzuchi, Y. Niimi, Y. Otani, and H. Takagi, Nat. Commun. **4**, 2893 (2013).

[14] M. Uchida, W. Sano, K. S. Takahashi, T. Koretsune, Y. Kozuka, R. Arita, Y. Tokura, and M. Kawasaki, Phys. Rev. B **91**, 241119(R) (2015).

[15] D.-Y. Kuo, J. K. Kawasaki, J. N. Nelson, J. Kloppenburg, G. Hautier, K. M. Shen, D. G. Schlom, and J. Suntivich, J. Am. Chem. Soc. **139**, 3473 (2017).

[16] Z. Liang, T. Li, M. Kim, A. Asthagiri, and J. F. Weaver, Science **356**, 299 (2017).

[17] Y. Sun, Y. Zhang, C.-X. Liu, C. Felser, and B. Yan, Phys. Rev. B **95**, 235104 (2017).

[18] S.-Y. Yang, H. Yang, E. Derunova, S. S. P. Parkin, B. Yan, and M. N. Ali, Adv. Phys. X **3**, 1414631 (2018).

[19] M. P. Seah and W. Dench, Surf. Interface Anal. **1**, 2 (1979).

[20] S. U. M. Khan, M. Al-Shahry, and W. B. Ingler, Science **297**, 2243 (2002).

[21] S.-D. Mo and W. Y. Ching, Phys. Rev. B **51**, 13023 (1995).

[22] See Supplemental Material at http://link.aps.org/supplemental/10.1103/PhysRevMaterials.3.064205 for data on sample characterization, polarization-dependent ARPES data, and a study of the effects of strain.

[23] P. Giannozzi, S. Baroni, N. Bonini, M. Calandra, R. Car, C. Cavazzoni, D. Ceresoli, G. L. Chiarotti, M. Cococcioni, I. Dabo, A. Dal Corso, S. de Gironcoli, S. Fabris, G. Fratesi, R. Gebauer, U. Gerstmann, C. Gougoussis, A. Kokalj, M. Lazzeri, L. Martin-Samos, N. Marzari, F. Mauri, R. Mazzarello, S. Paolini, A. Pasquarello, L. Paulatto, C. Sbraccia, S. Scandolo, G. Sclauzero, A. P. Seitsonen, A. Smogunov, P. Umari, and R. M. Wentzcovitch, J. Phys.: Condens. Matter **21**, 395502 (2009).

[24] D. R. Hamann, Phys. Rev. B **88**, 085117 (2013).

[25] J. P. Perdew, K. Burke, and M. Ernzerhof, Phys. Rev. Lett. **77**, 3865 (1996).

[26] P. Blaha, K. Schwarz, G. K. H. Madsen, D. Kvasnicka, J. Luitz, R. Laskowski, F. Tran, and L. D. Marks, *WIEN2k, An Augmented Plane Wave + Local Orbitals Program for Calculating Crystal Properties* (Karlheinz Schwarz, Vienna University of Technology, Austria, 2018).

[27] A. A. Mostofi, J. R. Yates, G. Pizzi, Y.-S. Lee, I. Souza, D. Vanderbilt, and N. Marzari, Comput. Phys. Commun. **185**, 2309 (2014).

[28] J. K. Kawasaki, M. Uchida, H. Paik, D. G. Schlom, and K. M. Shen, Phys. Rev. B **94**, 121104(R) (2016).

[29] P. K. Das, J. Sławińska, I. Vobornik, J. Fujii, A. Regoutz, J. M. Kahk, D. O. Scanlon, B. J. Morgan, C. McGuinness, E. Plekhanov, D. Di Sante, Y.-S. Huang, R.-S. Chen, G. Rossi, S. Picozzi, W. R. Branford, G. Panaccione, and D. J. Payne, Phys. Rev. Mater. **2**, 065001 (2018).

[30] J. M. Kahk, C. G. Poll, F. E. Oropeza, J. M. Ablett, D. Céolin, J.-P. Rueff, S. Agrestini, Y. Utsumi, K. D. Tsuei, Y. F. Liao, F. Borgatti, G. Panaccione, A. Regoutz, R. G. Egdell, B. J. Morgan, D. O. Scanlon, and D. J. Payne, Phys. Rev. Lett. **112**, 117601 (2014).

[31] L. M. Schoop, M. N. Ali, C. Straßer, A. Topp, A. Varykhalov, D. Marchenko, V. Duppel, S. S. P. Parkin, B. V. Lotsch, and C. R. Ast, Nat. Commun. **7**, 11696 (2016).

[32] N. P. Armitage, E. J. Mele, and A. Vishwanath, Rev. Mod. Phys. **90**, 015001 (2018).

[33] V. Strocov, J. Electron Spectrosc. Relat. Phenom. **130**, 65 (2003).

[34] L. S. Xie, L. M. Schoop, E. M. Seibel, Q. D. Gibson, W. Xie, and R. J. Cava, APL Mater. **3**, 083602 (2015).

[35] E. Emmanouilidou, B. Shen, X. Deng, T.-R. Chang, A. Shi, G. Kotliar, S.-Y. Xu, and N. Ni, Phys. Rev. B **95**, 245113 (2017).

[36] B. Feng, B. Fu, S. Kasamatsu, S. Ito, P. Cheng, C.-C. Liu, Y. Feng, S. Wu, S. K. Mahatha, P. Sheverdyaeva, P. Moras, M. Arita, O. Sugino, T.-C. Chiang, K. Shimada, K. Miyamoto, T. Okuda, K. Wu, L. Chen, Y. Yao, and I. Matsuda, Nat. Commun. **8**, 1007 (2017).

[37] R. Yu, Q. Wu, Z. Fang, and H. Weng, Phys. Rev. Lett. **119**, 036401 (2017).

[38] Q. Xu, Z. Song, S. Nie, H. Weng, Z. Fang, and X. Dai, Phys. Rev. B **92**, 205310 (2015).

[39] G. Bian, T.-R. Chang, R. Sankar, S.-Y. Xu, H. Zheng, T. Neupert, C.-K. Chiu, S.-M. Huang, G. Chang, I. Belopolski, D. S. Sanchez, M. Neupane, N. Alidoust, C. Liu, B. Wang, C.-C. Lee, H.-T. Jeng, C. Zhang, Z. Yuan, S. Jia, A. Bansil, F. Chou, H. Lin, and M. Z. Hasan, Nat. Commun. **7**, 10556 (2016).

[40] M. Neupane, I. Belopolski, M. M. Hosen, D. S. Sanchez, R. Sankar, M. Szlawska, S.-Y. Xu, K. Dimitri, N. Dhakal, P. Maldonado, P. M. Oppeneer, D. Kaczorowski, F. Chou, M. Z. Hasan, and T. Durakiewicz, Phys. Rev. B **93**, 201104(R) (2016).

[41] D. Takane, Z. Wang, S. Souma, K. Nakayama, C. X. Trang, T. Sato, T. Takahashi, and Y. Ando, Phys. Rev. B **94**, 121108(R) (2016).

[42] A. Topp, J. M. Lippmann, A. Varykhalov, V. Duppel, B. V. Lotsch, C. R. Ast, and L. M. Schoop, New J. Phys. **18**, 125014 (2018).

[43] S. A. Ekahana, S.-C. Wu, J. Jiang, K. Okawa, D. Prabhakaran, C.-C. Hwang, S.-K. Mo, T. Sasagawa, C. Felser, B. Yan, Z. Liu, and Y. Chen, New J. Phys. **19**, 065007 (2017).

[44] G. Bian, T.-R. Chang, H. Zheng, S. Velury, S.-Y. Xu, T. Neupert, C.-K. Chiu, S.-M. Huang, D. S. Sanchez, I. Belopolski, N. Alidoust, P.-J. Chen, G. Chang, A. Bansil, H.-T. Jeng, H. Lin, and M. Z. Hasan, Phys. Rev. B **93**, 121113(R) (2016).

[45] S. Li, Y. Liu, S.-S. Wang, Z.-M. Yu, S. Guan, X.-L. Sheng, Y. Yao, and S. A. Yang, Phys. Rev. B **97**, 045131 (2018).

[46] C. Chen, X. Xu, J. Jiang, S.-C. Wu, Y. P. Qi, L. X. Yang, M. X. Wang, Y. Sun, N. B. M. Schröter, H. F. Yang, L. M. Schoop, Y. Y. Lv, J. Zhou, Y. B. Chen, S. H. Yao, M. H. Lu, Y. F. Chen, C. Felser, B. H. Yan, Z. K. Liu, and Y. L. Chen, Phys. Rev. B **95**, 125126 (2017).

[47] V. Jovic, R. J. Koch, S. K. Panda, H. Berger, P. Bugnon, A. Magrez, K. E. Smith, S. Biermann, C. Jozwiak, A. Bostwick, E. Rotenberg, and S. Moser, Phys. Rev. B **98**, 241101(R) (2018).

[48] K. V. Shanavas, Z. S. Popović, and S. Satpathy, Phys. Rev. B **90**, 165108 (2014).

[49] D.-Y. Kuo, H. Paik, J. Kloppenburg, B. Faeth, K. M. Shen, D. G. Schlom, G. Hautier, and J. Suntivich, J. Am. Chem. Soc. **140**, 17597 (2018).

[50] E. Tsuji, A. Imanishi, K. ichi Fukui, and Y. Nakato, Electrochim. Acta **56**, 2009 (2011).

[51] W. D. Ryden, W. A. Reed, and E. S. Greiner, Phys. Rev. B **6**, 2089 (1972).

[52] J. J. Lin, S. M. Huang, Y. H. Lin, T. C. Lee, H. Liu, X. X. Zhang, R. S. Chen, and Y. S. Huang, J. Phys.: Condens. Matter **16**, 8035 (2004).

[53] P. R. Wallace, Phys. Rev. **71**, 622 (1947).

[54] N. Kumar, Y. Sun, N. Xu, K. Manna, M. Yao, V. Süss, I. Leermakers, O. Young, T. Förster, M. Schmidt, H. Borrmann, B. Yan, U. Zeitler, M. Shi, C. Felser, and C. Shekhar, Nat. Commun. **8**, 1642 (2017).

[55] X. Wang, X. Pan, M. Gao, J. Yu, J. Jiang, J. Zhang, H. Zuo, M. Zhang, Z. Wei, W. Niu, Z. Xia, X. Wan, Y. Chen, F. Song, Y. Xu, B. Wang, G. Wang, and R. Zhang, Adv. Electron. Mater. **2**, 1600228 (2016).

[56] R. Singha, A. K. Pariari, B. Satpati, and P. Mandal, Proc. Natl. Acad. Sci. USA **114**, 2468 (2017).

[57] T. Nan, T. J. Anderson, J. Gibbons, K. Hwang, N. Campbell, H. Zhou, Y. Q. Dong, G. Y. Kim, N. Reynolds, X. J. Wang, N. X. Sun, S. Y. Choi, M. S. Rzchowski, Y. B. Kim, D. C. Ralph, and C. B. Eom, arXiv:1808.06650.

[58] X. Xu, J. Jiang, W. J. Shi, V. Süß, C. Shekhar, S. C. Sun, Y. J. Chen, S.-K. Mo, C. Felser, B. H. Yan, H. F. Yang, Z. K. Liu, Y. Sun, L. X. Yang, and Y. L. Chen, Phys. Rev. B **99**, 195106 (2019).

Supplemental Information: Dirac nodal lines protected against spin-orbit interaction in IrO_2

J. N. Nelson,[1] J. P. Ruf,[1] Y. Lee,[1] C. Zeledon,[2] J. K. Kawasaki,[3] S. Moser,[4] C. Jozwiak,[5] E. Rotenberg,[5] A. Bostwick,[5] D. G. Schlom,[2,6] K. M. Shen,[1,6,*] and L. Moreschini[2,†]

[1]*Laboratory of Atomic and Solid State Physics, Department of Physics, Cornell University, Ithaca, New York 14853, USA*
[2]*Department of Materials Science and Engineering, Cornell University, Ithaca, New York 14853, USA*
[3]*Department of Materials Science and Engineering, University of Wisconsin, Madison, Wisconsin 53706, USA*
[4]*Physikalisches Institut, Universität Würzburg, D-97074 Würzburg, Germany*
[5]*Advanced Light Source, Lawrence Berkeley National Laboratory, Berkeley, California 94720, USA*
[6]*Kavli Institute at Cornell for Nanoscale Science, Ithaca, New York 14853, USA*

S1: Film Growth and Characterization

Thin films of IrO_2 were grown on single-crystal TiO_2 substrates by reactive oxide molecular beam epitaxy (MBE) in a dual-chamber Veeco GEN10 system. A combination of undoped, 0.05 wt % and 0.5 wt % Nb-doped TiO_2 substrates were used with no difference observed either in growth or in the ARPES data. A background pressure of 1×10^{-6} torr of distilled ozone was used and the substrate temperature was 300 °C. An Ir flux of 5×10^{12} - 1×10^{13} atoms/cm^2·s was supplied by an electron beam evaporator. *In situ* reflection high-energy electron diffraction (RHEED) was used to monitor the film growth. After each growth of IrO_2 a single ($\sim$1.5 Å thick) crystalline monolayer of TiO_2 was immediately deposited, in the same conditions, as protection for the *ex situ* ARPES measurements described below. Fluxes were calibrated using a quartz crystal microbalance (QCM) before growth and by RHEED oscillations during growth on TiO_2 (110). Growth on TiO_2 (001) did not display RHEED oscillations.

The structure of the resulting films was characterized through x-ray diffraction (Cu Kα). Figure 1(b) in the main text shows 2θ scans on both IrO_2 (001) and (110) indicating that both films are phase pure and exhibit thickness fringes indicating high quality crystalline growth with sharp interfaces.

The surfaces of films were characterized using atomic force microscopy (figure S1) showing atomically flat film growth on both surfaces of IrO_2 with RMS roughness of 0.68 Å on IrO_2(110) and 0.74 Å on IrO_2(001), both less than the height of a unit cell.

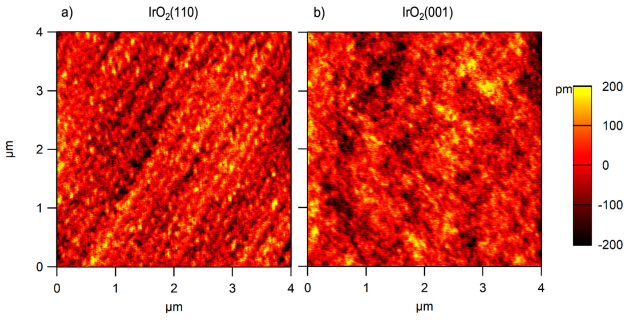

FIG. S1. Atomic force microscopy images a) IrO_2(110) and b) IrO_2(001).

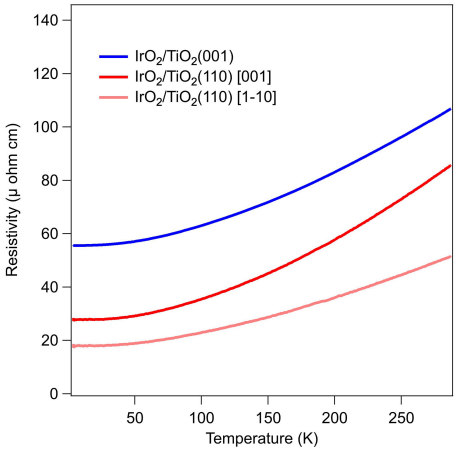

FIG. S2. Van der Pauw transport measurements on IrO_2 (110) (red) and IrO_2 (001) (blue).

Van der Pauw transport measurements (see Fig. S2) were performed on 10×10 mm films grown on undoped substrates, and show that the samples are metallic down to 4.2 K. For the IrO_2 (110) because the sample is inherently anisotropic due to the in equivalence of the directions $[1\bar{1}0]$ and [001] the resistivity was corrected using the Montgomery method [1, 2]. The higher resistance along [001] is likely due in part to the partial relaxation in this direction (as shown by x-ray diffraction in fig. S8) which may increase the scattering of the charge carriers due to disorder. The two in plane directions of the IrO_2(001) film are related by symmetry therefore the Newton-Raphson method was used to solve for the sheet resistance.

In Fig. S3 we show the Ti $2p$ signal measured on the IrO_2 films after the O_3 treatment mentioned in the text. The protective TiO_2 layer is not removed by the O_3 but its presence does not affect the ARPES data because of the $>$3 eV band gap.

S2: Photoemission

ARPES measurements were performed at the microARPES endstation of beamline 7.0.1 (MAESTRO), at

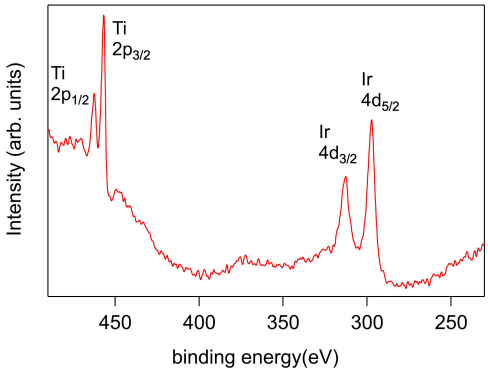

FIG. S3. Angle integrated X-ray photoemission on a representative IrO_2 /TiO_2 (001) sample, hν=600 eV.

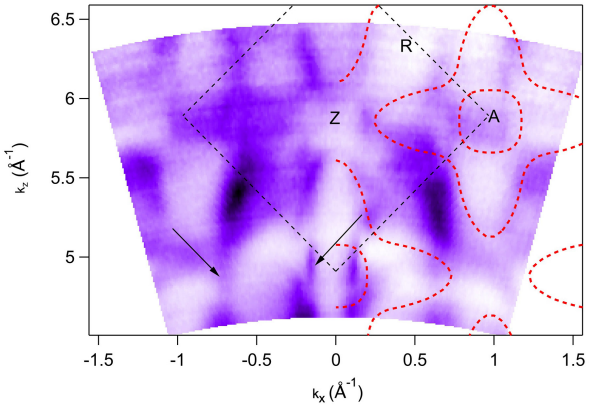

FIG. S4. k_z scan through the BZ edge of the IrO_2 (110) surface, with DFT predictions shown in red dashed lines, the BZ boundaries are shown as black dashed lines. The arrows point to spectral features that were previously ascribed to surface states [3].

the ALS, Lawrence Berkeley National Laboratory, using a Scienta R4000 electron analyzer. The combined (beamline + analyzer) energy resolution was between 15 meV and 25 meV depending on the photon energy used. Measurements were taken between 20K and 77 K but the samples showed no temperature dependence in that range. The measurement geometry is shown in fig. S5(a).

• *k_z dependence*: Figure S4 shows a k_z scan through the 3D BZ boundary measured on the IrO_2 (110) surface, with the results from DFT overlayed. This cut is equivalent to that of Fig. 2(f) of the main text on a (001) film, but it is here measured by varying the photon energy over approximately a full BZ. The characteristic four-leaf clover shape is clearly visible, symmetrically with respect to $k_x = 0$, but in this measurement, as opposed to Fig. 2(f), some additional intensity is present in other regions of the reciprocal space, as indicated by the arrows. The intensity appears to "leak" from the clover leaves into lower k_z values and shows that the spectral features present on the (110) surface [Fig. 2(b)], identified in Ref. 3 as surface states, are in fact artifacts due to k_z broadening from the hole-like bulk states. They are indeed present also in the theoretical Fermi surfaces shown in Fig.2(c,d) of the main text, where the k_z broadening has been included.

• *light polarization and matrix elements*: in a "pure" $J_{\rm eff}$ description of the Ir 5d levels, the orbital momentum L is not a good quantum number and therefore the five d electrons are equally distributed among the three t_{2g} orbital symmetries. As a consequence, in layered perovskites, where the departure from the $J_{\rm eff}$ model is small, the ARPES intensity shows hardly any modulation induced by the dipole matrix elements [4, 5]. The rutile structure of IrO_2 instead causes a substantial crystal field splitting and the orbital ordering is not negligible. The density of states shows a clear difference among the three t_{2g} orbitals [6]. This can be elegantly proven by ARPES, which shows characteristic intensity suppressions well documented, *e.g.*, in perovskite ruthenates [7], and absent instead in perovskite iridates [4, 5].

The experimental geometry used is shown in Fig. S5(a). The matrix elements depend on the orientations of the vector potential of the electromagnetic wave $\mathbf{A}$ and of the momentum of the electron $\mathbf{p}$. Namely, if the photoelectron is emitted in a reflection symmetry plane for the sample, the in-plane component of the vector potential $A_{\parallel}$ selects *even* initial states, whereas the perpendicular component $A_{\perp}$ selects *odd* initial states. These selection rules are strictly valid within the mirror plane, while the intensity is smoothly recovered outside it, where the parity of the states is ill-defined. We will use in the following capital letters for the rutile crystal axes and italic letters for the sample coordinates as defined throughout the paper, where xy is the surface plane and z is the surface normal.

It is common practice for the rutile structure to refer orbitals to a locally rotated coordinate system centered on each Ir site [9] (see Fig. S5(b)). In this scheme, X is always parallel to [001], Y is parallel to the orthogonal edge-sharing direction of the IrO_6 octahedral network (either [110] or [1$\bar{1}$0], Y and Y' in Fig. S5(b)), and Z is parallel to the corner-sharing direction of this network (either [1$\bar{1}$0] or [110], Z and Z' in Fig. S5(b)). This choice makes the most sense as the two different IrO_6 networks differ only by a 90° rotation about X and therefore Y and Z' (as well as Y' and Z) are locally equivalent [6, 9]. However, since here we are focusing on the parity of the orbitals we will refer them to global coordinates X, Y and Z, and the Wannierization routine employed will project the total density of states onto global d_{XY}, d_{XZ} and d_{YZ} orbitals. Note that, as an immediate consequence of the presence of two octahedral sublattices discussed above, in this basis the projection of the total wavefunction onto d_{XY} and d_{XZ} is equal by geometry, minus a phase factor due to the translation vector between the two sublattices. We show in Fig. S5(c,d) the Fermi surface in the ΓMAZ plane measured on a (110) film (notice that in this orientation $x = Y$, $y = X$ and $z = Z$), with both p and s polarization, and in Fig. S5(e) the calculated orbital projection onto d_{YZ} orbitals. Both electron-like and hole-like states

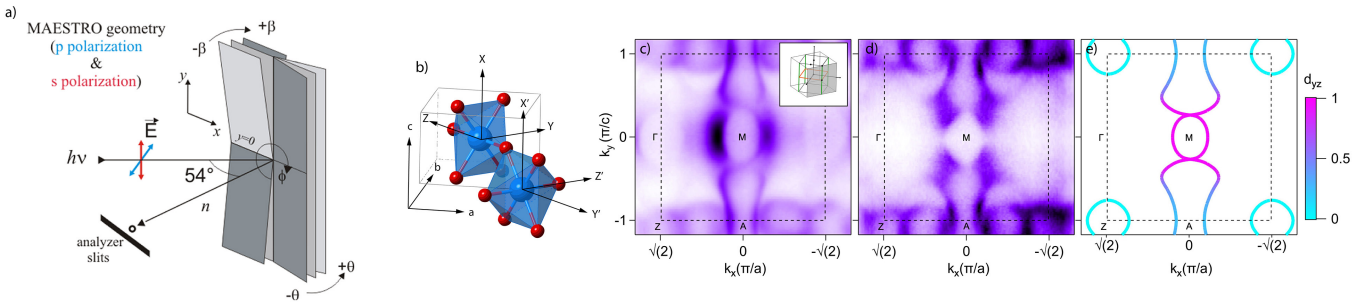

FIG. S5. (a) experimental geometry used for the ARPES experiments. the angles θ and β move along k_x and k_y, respectively. (b) unit cell of IrO_2 showing the two octahedra orientations with the respective local coordinates. (c,d) Fermi surface measured on a (110) film for the ΓMAZ plane, at $h\nu$=84 eV, with p and s polarization. (e) calculated projection of the total spectral weight for the same k_z value as in (c,d), on the global d_{YZ} orbitals (see text). The color codes the d_{YZ} fraction of the total spectral weight.

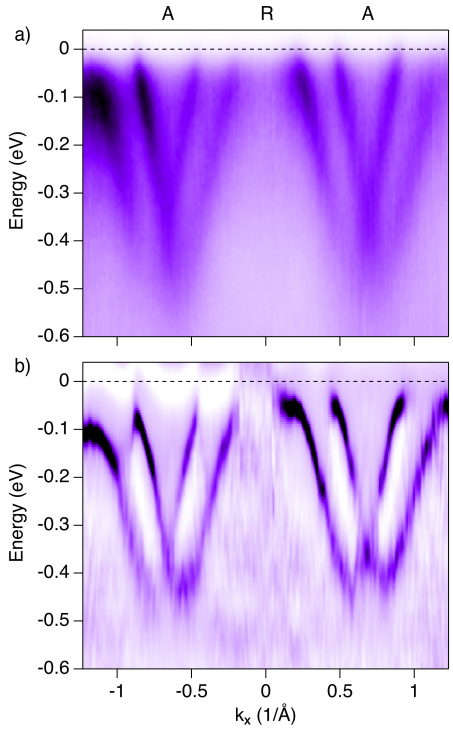

FIG. S6. (a) Dispersion along A-R-A measured at 100 eV on the IrO_2(001) surface, and (b) corresponding curvature plot [8].

close to M clearly have almost exclusively d_{YZ} character.

- *for p polarization:* at normal emission (M), **A** is *even* with respect to the xz plane. The d_{YZ} states are *even* as well and therefore they are visible along the x axis. Along the y axis, the mirror plane to consider is yz. With respect to yz **A** has both *even* and *odd* components, with $(A_{\parallel}/A_{\perp})^2 \simeq 2$, and d_{YZ}, which is *odd* with respect to yz, can again be observed but substantially suppressed. In Fig. S5(c) the spectral weight is indeed strong along x and weaker yet present along y.

- *for s polarization:* at normal emission (M), **A** is *odd* with respect to the xz plane. The d_{YZ} states are *even* instead and therefore they are suppressed along the x axis. Along the y axis, the mirror plane to consider is yz. With respect to yz **A** is now *even*. d_{YZ} instead is *odd* and therefore it cannot be excited. In Fig. S5(d) the spectral weight is indeed completely suppressed along both x and y.

• *A-M nodal line crossing at A*: the nodal line along A-M was shown in the vicinity of the Fermi level crossing in Fig. 3(b-g), on the (110) surface. The matrix elements there are not ideal for showing the crossing point approaching A, where the ARPES intensity is fainter. We show instead in Fig. S6(a) the dispersion along a cut taken at 45 degrees from those in Fig. 3, along the A-R-A line. The cut was measured at 100 eV on the IrO_2(001) surface, in a favorable direction for observing the nodal line crossing. This is even more readily visible in the curvature plot [8] of Fig. S6(b), and proves the persistence of a Dirac node through the whole section of the A-M line where this lies below the Fermi level, in the occupied states.

• k_z *broadening*: as mentioned in the main text, the finite escape depth of photoelectrons causes an intrinsic uncertainty in the value of k_z measured by ARPES, of the order of $1/\lambda$ where λ is the mean free path of the electrons in the solid ad a given kinetic energy. As a consequence, when measuring a band crossing in bulk states an apparent gap can be introduced in the data by this unavoidable artifact. Fig. S7(a-f) presents the evolution of the crossing points along the A-M line, as shown in Fig. 3(j-o), for a k_z at 0.1 $Å^{-1}$ from the ΓXM high symmetry plane containing the nodal line. In Fig. S7(a) the apparent gap is as large as ∼80 meV.

S3. Effects of Strain

Reciprocal space maps were measured using a lab based x-ray diffraction (Cu Kα) equipped with a pixel array detector, as shown in Fig. S8. The measured lattice constants are summarized in table S1. In IrO_2(001), where the in-plane [100] and [010] axes are equivalent, the films are coherently and positively strained in plane (∼2.0%), a weak and broad feature near the bulk peak (red triangle in fig S8 c) may indicate that the near surface region is partially relaxed (strain of ∼0.1%). The normal [001] axis shows a compressive ∼-1.2%

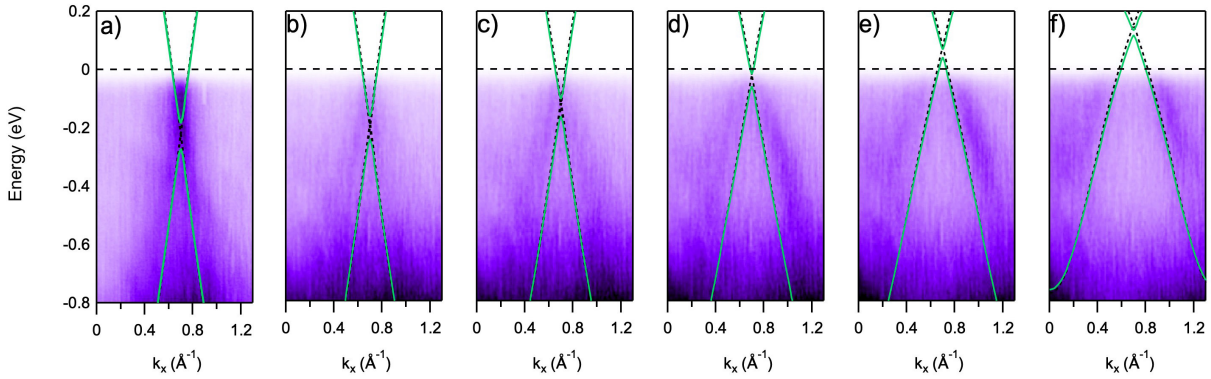

FIG. S7. (a-f) Same data shown in Fig. 3(j-o) with the DFT dispersion superposed for $k_{[001]}$ corresponding to the high symmetry plane (black dashed lines) and at 0.1 Å^{-1} from the high symmetry plane (full green line).

	IrO_2 bulk Å[10]	TiO_2 bulk Å[11]	IrO_2/TiO_2(001) Å(strain)	IrO_2/TiO_2(110) Å(strain)
a	4.5051	4.594	4.594 (2.0%)	
c	3.1586	2.959	3.12 (-1.2%)	
d_{110}	3.1856	3.248		3.21 (0.8%)
$d_{1\bar{1}0}$	3.1856	3.248		3.25 (2.0%)
d_{001}	3.1586	2.959		3.0 (-5.0 %)

TABLE S1. Lattice constants and strain states of IrO_2 and TiO_2 bulk and thin films. Strain is defined as (a_f - a_b)/a_b where a_f is the film lattice parameter and a_b is the bulk lattice parameter [12]. Due to the uncertainty in determining d_{001} in the IrO_2 (110) sample because two peaks are present in the film we calculate it based on assuming a Poisson ratio [13] of 0.24 found for the IrO_2 (001) film and find that this calculated lattice constant is consistent with the measured peak.

strain compared to bulk IrO_2 , extracted from the $\theta/2\theta$ scan of Fig. 1(b). In IrO_2(110), for the in-plane directions the data indicate that the films are coherently and positively strained ($\sim$2%) along [1$\bar{1}$0], and partially relaxed along [001], with two broad peaks indicating that part of the film, likely close to the interface, is compressively strained by $\sim$-5.0% and another region, likely near the surface, by $\sim$-3.6% . Due to the uncertainty in determining the $d_{[001]}$ lattice spacing we calculate it using the Poisson ratio (Ref. 13) extracted for the IrO_2 (001) films (0.24) and find $\sim$3.0 Å (-5.0% strain). The out-of-plane [110] lattice constant is slightly positively strained ($\sim$0.8%). We use these lattice parameters for the DFT calculations under strain (see below).

As a result of the epitaxial strain discussed above, (001) films, where the two in plane [100] and [010] axes are structurally equivalent, preserve the space group n.136 ($P4_2/mnm$) with nonsymmorphic symmetry, and therefore the nodal lines. On (110) films, instead, the in plane [1$\bar{1}$0] axis is stretched by $\sim$2%, the in plane [001] axis is compressed by 3.6-5.0 % while the out plane [110] is stretched by $\sim$0.8%. Both the nonsymmorphic terms in the crystal symmetry are lost and so are the A-M and X-M nodal lines.

To simulate the electronic structure of (110)-oriented films, we adopted a base-centered orthorhombic crystal structure (space group n.65, $Cmmm$) with lattice constants of the conventional unit cell equal to $2d_{110}$, $2d_{1\bar{1}0}$, and c. The primitive unit cell in this structure contains the same number of Ir and O atoms as the parent rutile unit cell, so there is no apparent doubling and/or folding of the bands. Finally, because the oxygen positions in thin films of IrO_2 have not been determined experimentally, for all DFT calculations we kept the internal positional parameter $x_{\rm O}$ (and also $y_{\rm O}$ in the case of $Cmmm$ structures) that determines the two (four) inequivalent Ir-O bond lengths fixed to its bulk value of 0.3100 [10]. We show in Fig. S9(a) the resulting Fermi surface through Γ from DFT, and in Fig. S9(b-g) the calculated dispersion along A-M for the same ARPES cuts of Fig.3(b-g). The full comparison of the calculated dispersion for the bulk and strained structure is shown in Fig. S9(h,i). The average value of the expected splitting along X-M and A-M is $\sim$50 meV but it can be as large as $\sim$100 meV.

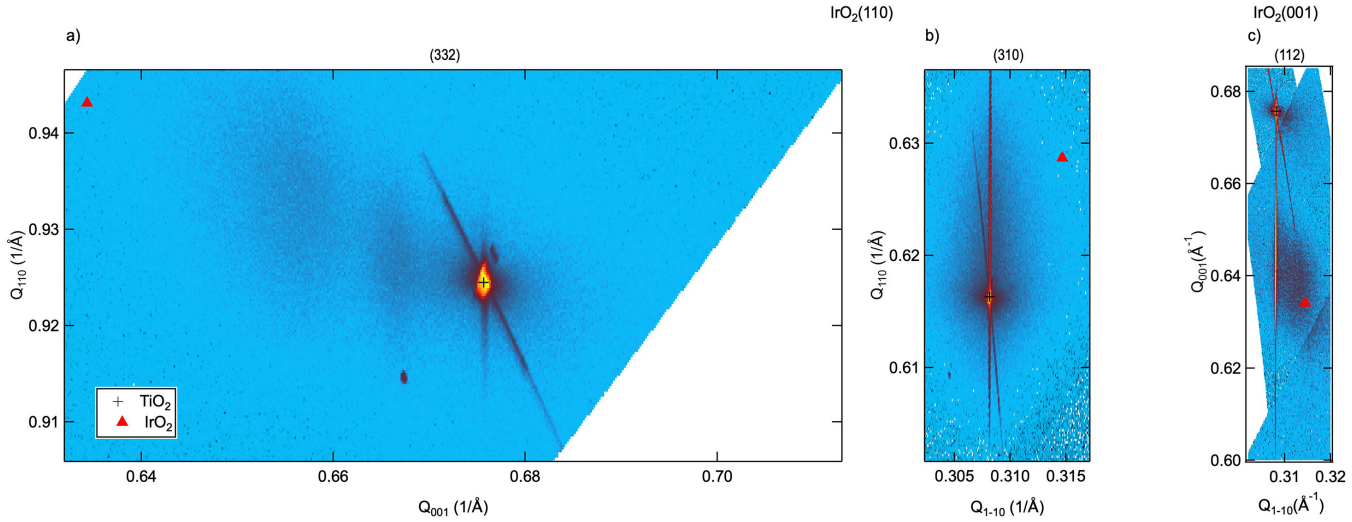

FIG. S8. Reciprocal space maps of IrO_2 (110) films (a,b) and IrO_2 (001) films (c) as obtained by x-ray diffraction. The red triangles denote the position of the bulk IrO_2 peak [10] while the black crosses show the position of the bulk TiO_2 peaks [11]. Only one panel is shown for the IrO_2 (001) films because the two in-plane axes are equivalent by geometry.

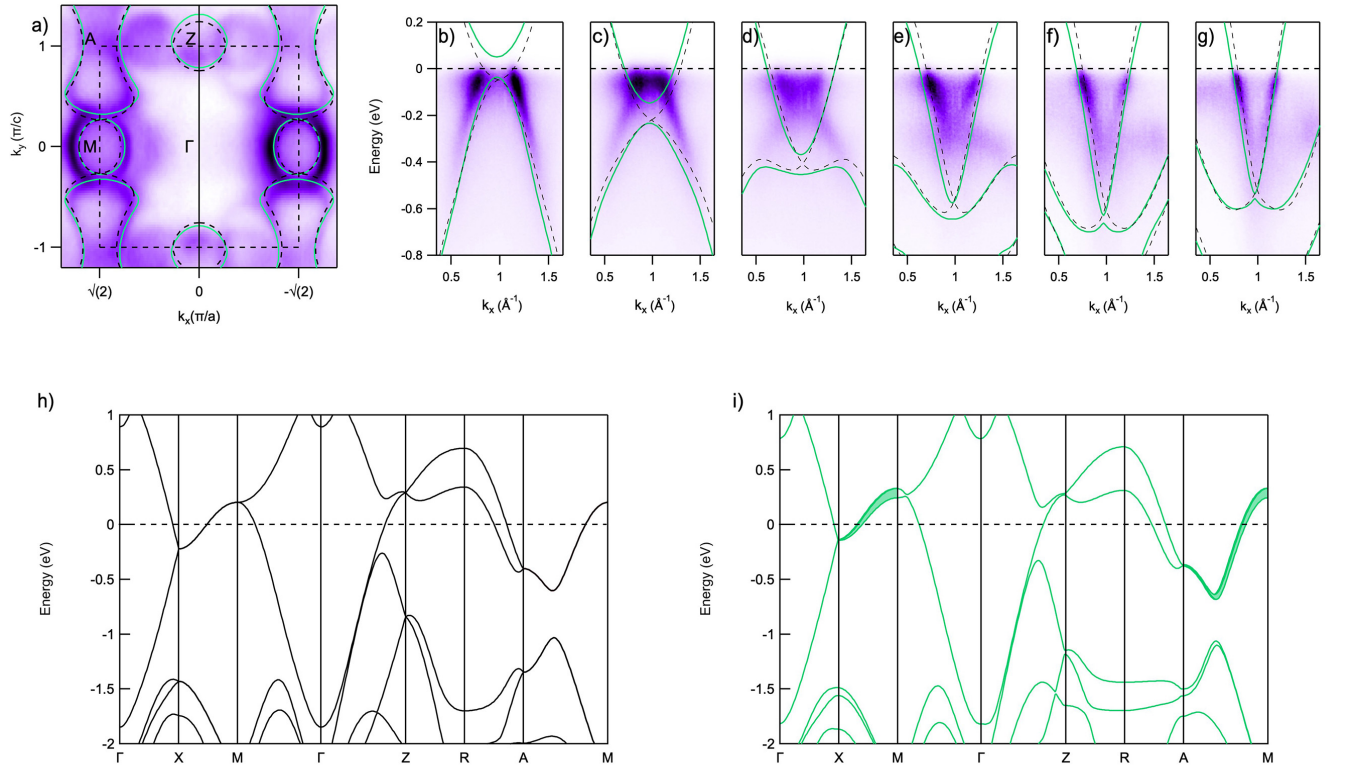

FIG. S9. (a) Fermi surface measured at Γ on a (110), same as in Fig. 2(c). The Fermi surface calculated for bulk IrO_2 and for the strained structure are superposed as black dashed lines and full green lines, respectively. (b-g) same ARPES cuts and theoretical dispersions as in Fig.3(b-g) with the DFT calculations for the strained films superposed. (h,i) Comparison of the DFT results for the bulk crystal and for the strained structure along all the high symmetry lines of the 3D BZ.

* kmshen@cornell.edu
† lmoreschini@cornell.edu

[1] C. A. M. dos Santos, A. de Campos, M. S. da Luz, B. D. White, J. J. Neumeier, B. S. de Lima, and C. Y. Shigue, Journal of Applied Physics **110**, 083703 (2011).
[2] H. C. Montgomery, Journal of Applied Physics **42**, 2971 (1971).
[3] P. K. Das, J. Sławińska, I. Vobornik, J. Fujii, A. Regoutz, J. M. Kahk, D. O. Scanlon, B. J. Morgan, C. McGuinness, E. Plekhanov, D. Di Sante, Y.-S. Huang, R.-S. Chen, G. Rossi, S. Picozzi, W. R. Branford, G. Panaccione, and D. J. Payne, Phys. Rev. Materials **2**, 065001 (2018).
[4] B. J. Kim, H. Jin, S. J. Moon, J.-Y. Kim, B.-G. Park, C. S. Leem, J. Yu, T. W. Noh, C. Kim, S.-J. Oh, J.-H. Park, V. Durairaj, G. Cao, and E. Rotenberg, Phys. Rev. Lett. **101**, 076402 (2008).
[5] S. Moser, L. Moreschini, A. Ebrahimi, B. D. Piazza, M. Isobe, H. Okabe, J. Akimitsu, V. V. Mazurenko, K. S. Kim, A. Bostwick, E. Rotenberg, J. Chang, H. M. Ronnow, and M. Grioni, New Journal of Physics **16**, 013008 (2014).
[6] J. M. Kahk, C. G. Poll, F. E. Oropeza, J. M. Ablett, D. Céolin, J.-P. Rueff, S. Agrestini, Y. Utsumi, K. D. Tsuei, Y. F. Liao, F. Borgatti, G. Panaccione, A. Regoutz, R. G. Egdell, B. J. Morgan, D. O. Scanlon, and D. J. Payne, Phys. Rev. Lett. **112**, 117601 (2014).
[7] H. Iwasawa, Y. Yoshida, I. Hase, S. Koikegami, H. Hayashi, J. Jiang, K. Shimada, H. Namatame, M. Taniguchi, and Y. Aiura, Phys. Rev. Lett. **105**, 226406 (2010).
[8] P. Zhang, P. Richard, T. Qian, Y.-M. Xu, X. Dai, and H. Ding, Review of Scientific Instruments **82**, 043712 (2011).
[9] V. Eyert, Annalen der Physik **11**, 650 (2002).
[10] A. A. Bolzan, C. Fong, B. J. Kennedy, and C. J. Howard, Acta Crystallographica Section B **53**, 373 (1997).
[11] C. J. Howard, T. M. Sabine, and F. Dickson, Acta Crystallographica Section B **47**, 462 (1991).
[12] M. Henini, *Molecular Beam Epitaxy: From Research to Mass Production* (Elsevier Science, 2012).
[13] D. Bowen and B. Tanner, *High Resolution X-Ray Diffractometry And Topography* (CRC Press, 2005).